materials

MDPI

Article

Hollow Hemispherical Lithium Iron Silicate Synthesized by an Ascorbic Acid-Assisted Hydrothermal Method as a Cathode Material for Li Ion Batteries

Huaifu Li [1], Yunsong Li [2,*], Xuan Cheng [1,3,*] and Chaoyang Gong [1]

[1] Department of Materials Science & Engineering, College of Materials, Xiamen University, Xiamen 361005, China; 20720171150018@stu.xmu.edu.cn (H.L.); gcy@xmu.edu.cn (C.G.)
[2] School of Materials Science and Engineering, Northwestern Polytechnical University, Xi'an 710072, China
[3] Fujian Key Laboratory of Advanced Materials, Xiamen University, Xiamen 361005, China
* Correspondence: ysli@xmu.edu.cn (Y.L.); xcheng@xmu.edu.cn (X.C.)

Abstract: High-capacity and high-voltage cathode materials are required to meet the increasing demand for energy density in Li ion batteries. Lithium iron silicate (Li_2FeSiO_4) is a cathode material with a high theoretical capacity of 331 mAh·g^{-1}. However, its poor conductivity and low Li ion diffusion coefficient result in poor capability, hindering practical applications. Morphology has an important influence on the properties of materials, and nanomaterials with hollow structures are widely used in electrochemical devices. Herein, we report a novel hollow hemispherical Li_2FeSiO_4 synthesized by a template-free hydrothermal method with the addition of ascorbic acid. The hollow hemispherical Li_2FeSiO_4 consisted of finer particles with a shell thickness of about 80 nm. After carbon coating, the composite was applied as the cathode in Li ion batteries. As a result, the hollow hemispherical Li_2FeSiO_4/C exhibited a discharge capacity as high as 192 mAh·g^{-1} at 0.2 C, and the average capacities were 134.5, 115.5 and 93.4 mAh·g^{-1} at 0.5, 1 and 2 C, respectively. In addition, the capacity increased in the first few cycles and then decayed with further cycling, showing a warm-up like behavior, and after 160 cycles the capacities maintained 114.2, 101.6 and 79.3 mAh·g^{-1} at 0.5, 1 and 2 C, respectively. Such a method of adding ascorbic acid in the hydrothermal reaction can effectively synthesize hollow hemispherical Li_2FeSiO_4 with the enhanced electrochemical performance.

Keywords: Li ion batteries; cathode material; hollow hemispherical Li_2FeSiO_4; ascorbic acid

Citation: Li, H.; Li, Y.; Cheng, X.; Gong, C. Hollow Hemispherical Lithium Iron Silicate Synthesized by an Ascorbic Acid-Assisted Hydrothermal Method as a Cathode Material for Li Ion Batteries. *Materials* **2022**, *15*, 3545. https://doi.org/10.3390/ma15103545

Academic Editor: Alessandro Dell'Era

Received: 23 March 2022
Accepted: 13 May 2022
Published: 16 May 2022

1. Introduction

Rechargeable batteries with a high energy density, high power density, good rate performance, long cycle life and a reasonable price are an important part of sustainable energy, and their gradual application in energy-consuming devices will significantly alleviate the environmental problems caused by fuel systems [1]. Li ion batteries are mature commercial rechargeable batteries, but their energy density, cycle life and safety performance need to be improved to meet the needs of higher energy density, longer battery life and safer performance. Cathode materials dominate the energy density of Li ion batteries, and commercial cathode materials $LiCoO_2$ and $LiFePO_4$ deliver capacities below 170 mAh·g^{-1}. Therefore, it is necessary to develop cathode materials with the potential to release higher capacities. Li_2FeSiO_4 has the advantage of a high theoretical capacity (331 mAh·g^{-1}), environmental friendliness and a relatively low cost [2], and its cycle performance is better than that of Li_2MnSiO_4 [3] since Li_2MnSiO_4 suffers from the crystal structural deformation caused by the Jahn-Teller effect of Mn^{3+} [4,5]. However, the low ionic diffusion coefficient (~16 × 10^{-16} cm^2/s) [6] and poor electronic conductivity (~6 × 10^{-14} S·cm^{-1}) [7] make it difficult for Li_2FeSiO_4 to deintercalate more than one Li ion (corresponding to 165 mAh·g^{-1}) at room temperature. In addition, the deintercalation of the second Li ion in Li_2FeSiO_4 originates from the oxidation of O^{2-} rather than the oxidation of Fe^{3+} [2,8,9], since the

oxidation potential of Fe^{3+}/Fe^{4+} is higher than 4.8 V, O^{2-} with a lower oxidation potential oxidized first [2,10,11]. To achieve a high capacity, most of the modified Li_2FeSiO_4 materials have been prepared by the strategies of ion doping [12–14], morphology control [15–17], preparation of nanocrystals [18–20] or the methods combined with carbon coating [21–26].

Material morphology has an important influence on the performance, and a high porosity morphology endows the material with efficient electrolyte penetration and fast electron transport [27]. Hydrothermal synthesis enables the fabrication of Li_2FeSiO_4 nanostructures with well-defined shapes and fine-tuned dimensions [27]. Hollow spherical structures have the advantage of a large specific surface area, large voids, and strong mass transfer ability, which can improve the performance of low-kinetic, high-capacity cathode materials [28,29]. However, the hydrothermally synthesized Li_2FeSiO_4/C composites with hollow spherical structures exhibited capacities lower than 180 $mAh \cdot g^{-1}$ at 0.1 C and 165 $mAh \cdot g^{-1}$ at 0.2 C [16,24,30–33]. The discharge capacity of hollow spherical Li_2FeSiO_4 synthesized by a hydrothermal method was 120 $mAh \cdot g^{-1}$ at 0.1 C and less than 40 $mAh \cdot g^{-1}$ at 2 C [16], and that of hollow mesocrystal Li_2FeSiO_4 decayed from 162 to 150 $mAh \cdot g^{-1}$ after six cycles (55 °C, 1/50 C) [34].

In this work, a novel hollow hemispherical Li_2FeSiO_4 was synthesized by a hydrothermal method with the addition of ascorbic acid. It has been found that ascorbic acid inhibited the oxidation of Fe^{2+} and reduced the particle size [35], and acted as a reducing agent [34,36]. Different to the previous studies, we demonstrate that the ascorbic acid significantly alters the particle morphology, enabling primary particles to self-assemble into hollow hemispherical structures with the enhanced electrochemical performance.

2. Materials and Methods

2.1. Materials Synthesis

The materials were synthesized by a hydrothermal method. A typical synthesis process is as follows. 0.02 mol $FeCl_2 \cdot 4H_2O$ (99.7%, Tianjin Guangfu Fine Chemical Research Institute, Tianjin, China) was dissolved in a mixed solution of 10 mL ethylene glycol and 50 mL deionized water to form a light green solution, and then 0.02 mol hydrophilic SiO_2 (99.8%, Shanghai Macklin Biochemical Co., Ltd., Shanghai, China) was slowly added and stirred evenly. Then, 0.0031 mol ascorbic acid ($C_6H_8O_6$, 99.7%, Xilong Scientific Co., Ltd., Shantou, China) was added, and finally, 0.12 mol $LiOH \cdot H_2O$ (Sinopharm Chemical Reagent Co., Ltd., Shanghai, China) was added, and stirred to form a dark green suspension. The suspension was transferred to a reaction kettle, heated from room temperature to 160, or 180 or 200 °C, and maintained for 12 h to obtain a grey sediment. The sediment was washed with alcohol and deionized water, and was centrifuged to obtain a yellow solid, which was then vacuum-dried at 80 °C for 6 h. Three samples obtained after hydrothermal reactions at 160, 180 and 200 °C are denoted as LFS160, LFS180 and LFS200, respectively. A sample obtained after a hydrothermal reaction without the addition of ascorbic acid at 200 °C is denoted as nano-LFS200. The LFS200 (or nano-LFS200) was mixed with sucrose (with a mass ratio of 1:2) in a beaker containing 10 mL deionized water and 10 mL ethanol, and the mixture was magnetically stirred at 80 °C. After solvent evaporation, a solid was collected and then calcined at 600 °C for 10 h in a nitrogen atmosphere to obtain LFS600 (or nano-LFS600).

2.2. Materials Characterization

Powder X-ray diffraction (XRD) patterns in the range of 2θ = 10–80° ($10° \cdot min^{-1}$) were recorded on an X-ray diffractometer (Ultima-IV, Rigaku, Tokyo, Japan) using Cu Kα radiation (λ = 0.154 nm) to study the phase composition and crystal structure of the materials. Morphological and microstructural observations were conducted by a field emission scanning electron microscope (FE-SEM, S-4800, Hitachi, Tokyo, JapanJapan), and a transmission electron microscope (TEM, Talos F200S, FEI, Eindhoven, Netherlands) equipped with an energy-dispersive X-ray spectrometer (EDX, Super-X, FEI, Eindhoven, Netherlands). Selected area electron diffraction (SAED) and high-resolution transmission

electron microscopic (HRTEM) and EDX mapping measurements were performed on the transmission electron microscope operated at 200 kV.

2.3. Electrodes Fabrication and Electrochemical Tests

Electrodes were fabricated by scribbling a mixture of the as-prepared LFS600 (or nano-LFS600), super-P and PVDF (a mass ratio of 8:1:1) on an Al foil, and an appropriate amount of N-methyl-2-pyrrolidone (NMP) was used as a solvent for the mixture. The electrodes were dried in a vacuum oven at 60 °C for 12 h. Cyclic charge–discharge measurements were performed on 2016-type coin cells at 30 °C in a potential window of 1.5–4.8 V versus Li/Li^+ using a Land BT-2000 test system (LAND Electronic Co., Ltd., Wuhan, China). The coin cells were assembled in an Ar-filled glovebox (Mbraun, Garching, Germany). An electrode was used as the cathode, a sheet of lithium metal was used as the anode, and a polypropylene membrane (Celgard 2500) was used as the separator. The electrolyte in the cells was composed of 1 M $LiPF_6$ dissolved in ethylene carbonate (EC), ethyl methyl carbonate (EMC) and dimethyl carbonate (DMC) (a volume ratio of 1:1:1) with 2% fluoroethylene carbonate (FEC). Electrochemical impedance spectroscopic (EIS) data were collected with an Autolab PGSTAT101 (Metrohm, Barendrecht, Netherlands) in the frequency range from 100 kHz to 0.1 Hz at an amplitude of 10 mV.

3. Results and Discussion

3.1. Structural Analysis

XRD patterns of the as-prepared samples are presented in Figure 1. The standard lines of monoclinic Li_2FeSiO_4 ($P2_1/n$ space group, PDF#97-024-6132) and orthorhombic Li_2FeSiO_4 ($Pmn2_1$ space group, PDF#97-016-1306) are also included for comparison. The results show that the orthorhombic Li_2FeSiO_4 structure was formed through hydrothermal reactions at 160, 180 and 200 °C, which is consistent with that of the Li_2FeSiO_4 obtained by the hydrothermal reaction at 200 °C without adding ascorbic acid [37]. The characteristic diffraction peaks observed from LFS600 in Figure 1 were ascribed to the (110) and (112) crystal planes of monoclinic Li_2FeSiO_4 ($P2_1/n$ space group), indicating a phase evolution from orthorhombic to monoclinic [37].

SEM images given in Figure 2a–f demonstrate that the LFS160, LFS180 and LFS200 exhibited a hollow hemispherical morphology. Figure 2e indicates that hollow hemispheres were composed of smaller nanoparticles. Particle size distribution diagrams shown in Figure S1 revealed the average sizes of 200–250, 250–320 and 450–550 nm for the LFS160, LFS180 and LFS200, respectively, were based on 100 particles on each sample. The higher the temperature, the larger the particle size. The inset in Figure 2c presents the morphology of sample nano-LFS200, obtained by the hydrothermal synthesis without ascorbic acid, and the relatively fine nanoparticles were observed. The results show that ascorbic acid changed the morphology, promoting self-assembly of primary particles into secondary hollow hemispherical particles. Ascorbic acid was used as a reducing agent in the hydrothermal synthesis of Li_2FeSiO_4 [34,36], and could reduce the particle sizes of Li_2FeSiO_4 [35] and Ag [38]. Moreover, ascorbic acid could regulate the particle self-assembly behavior of Li_2FeSiO_4. Figure 2g shows that the LFS600 exhibited a hollow hemispherical structure with a shell thickness of about 80 nm. EDX mapping images (Figure 2h–k) reveal that the elements of Fe, Si and O were uniformly distributed on the hollow hemispherical particle that was uniformly coated by C. A SAED image (Figure 3a) shows that the diffraction spots with distances of 5.37, 3.65, 3.13, 2.81, 2.68, 2.48 and 1.87 Å from the diffraction center are ascribed to the (101), (111), $(\bar{2}02)$, (112), $(\bar{3}01)$, (020) and $(\bar{3}21)$ crystal planes, respectively. The lattice fringes with a lattice spacing of 2.52 Å (Figure 3b) are assigned to the (020) plane. The diffraction spots in the FFT image (Figure 2c) are ascribed to the $(\bar{3}01)$, (020) and $(\bar{3}21)$ planes of monoclinic Li_2FeSiO_4. The observed (112) crystal plane of monoclinic Li_2FeSiO_4 indicates that the obtained LFS600 is predominated by monoclinic Li_2FeSiO_4, which confirms the results of XRD.

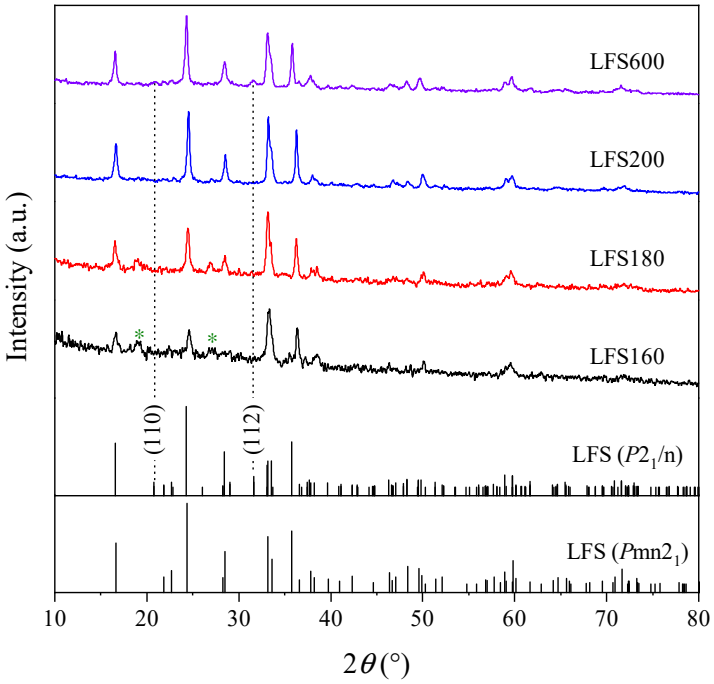

Figure 1. XRD patterns of the as-prepared Li_2FeSiO_4 samples. The diffraction peaks marked with an asterisk "*" represent the impure phase of Li_2SiO_3. The standard lines of monoclinic Li_2FeSiO_4 ($P2_1/n$ space group, PDF#97-024-6132) and orthorhombic Li_2FeSiO_4 ($Pmn2_1$ space group, PDF#97-016-1306) are included for comparison.

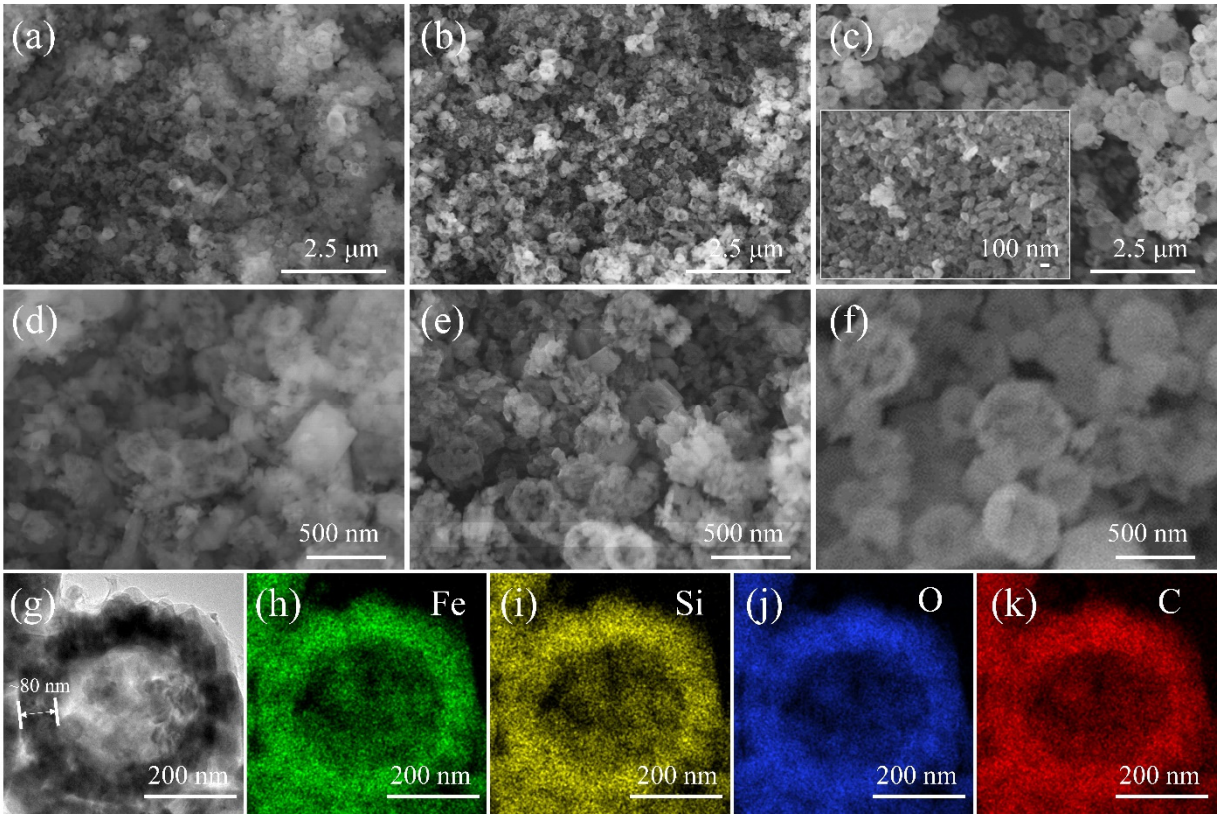

Figure 2. Morphologies of the Li_2FeSiO_4 samples. (**a**–**f**) SEM images of LFS160 (**a**,**d**), LFS180 (**b**,**e**) and LFS200 (**c**,**f**) (the inset in (**c**) is nano-LFS200). (**g**) TEM image and (**h**–**k**) EDX mapping images of Fe, Si, O and C for LFS600.

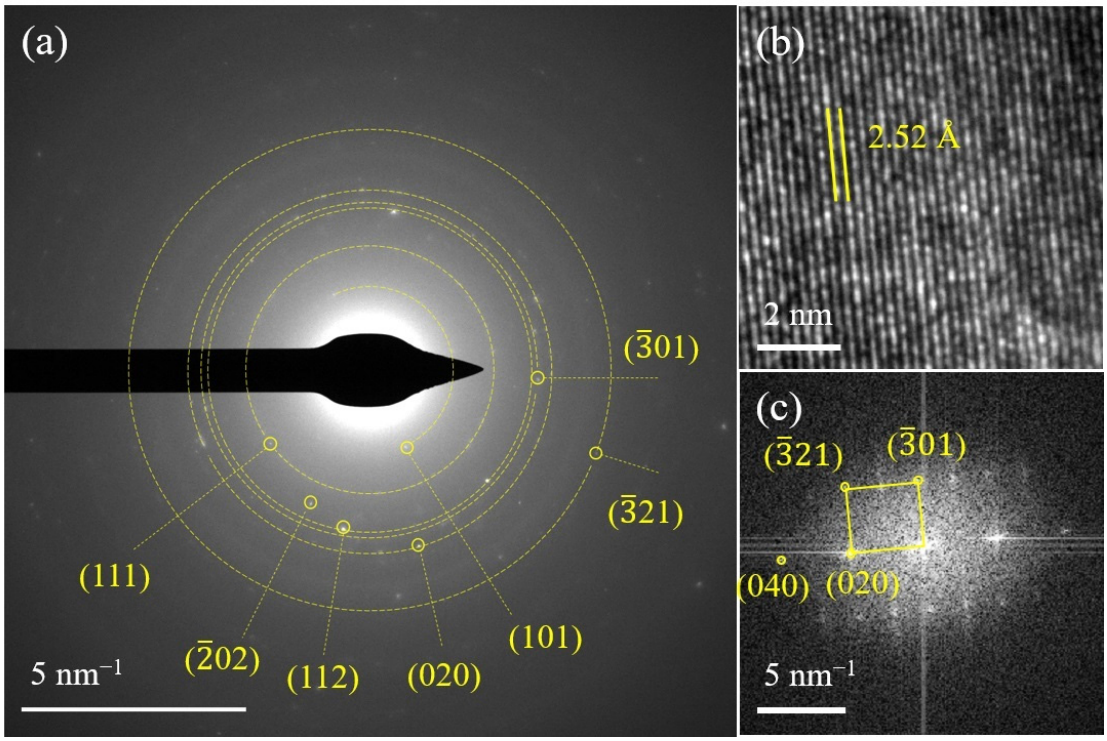

Figure 3. Microstructure characterization of LFS600. (**a**) SAED, (**b**) HRTEM and (**c**) FFT images.

3.2. Electrochemical Performance

Considering that the samples LFS160 and LFS180 contained an impure phase of Li_2SiO_3 (Figure 1), and their particle development degree (Figure 2d,e) was lower than that of LFS200 (Figure 2f), the follow-up study was only focused on the LFS200. The hydrothermally synthesized Li_2FeSiO_4 precursors commonly exhibit poor conductivity, and the carbon-coating and calcination are necessary for the electrochemical performance measurements [16,39–41]. Thus, the LFS200 sample was further mixed with sucrose and calcined at 600 °C to improve the conductivity (denoted as LFS600).

The charge–discharge curves of LFS600 are shown in Figure 4a. The first charge curve showed a voltage plateau at 3.2 V, attributed to Fe^{2+}/Fe^{3+} oxidation [42]. When the voltage exceeded 4.2 V, another voltage plateau was formed due to the O^{2-} oxidation [43], which is similar to those caused by the oxidation of O^{2-} on Li-rich cathode materials [44,45] and $Li_{1.25}Nb_{0.25}Fe_{0.50}O_2/C$ [46]. The first discharge curve became smooth at ~3.3 V, and then a plateau was formed, which is caused by the Fe^{3+}/Fe^{2+} reduction. The discharge plateau corresponding to the reduction peak at ~2.74 V in the differential capacity curve is presented in Figure 4c. The 2nd and 10th charging curves show a decreased curvilinear polarization, ostensibly rising from a capacity increase. Compared with the hollow spherical Li_2FeSiO_4 reported previously [16], the hollow hemispherical Li_2FeSiO_4 prepared with the addition of ascorbic acid exhibited a smaller curvilinear polarization.

Rate performance of the LFS600 (Figure 4b) show that the discharge capacity at 0.2 C increased from 110.1 mAh·g^{-1} (1st) to 163.4 mAh·g^{-1} (10th), which is ostensibly caused by the decreased curvilinear polarization, which is essentially attributed to the material activation [47]. The average discharge capacities at 0.5, 1 and 2 C were 134.5, 115.5 and 93.4 mAh·g^{-1}, respectively, while those of the nano-LFS600 (without ascorbic acid) were 121.9, 110.5 and 96.9 mAh·g^{-1}, respectively (Figure S2). Both the LFS600 and nano-LFS600 delivered a better performance than those of the nanoparticles sized 50–100 nm (135, 117 and 87 mAh·g^{-1} at 0.2, 0.5 and 1 C, respectively) [48]. When the rate changed from 2 C to 0.2 C, the discharge capacity increased from 172.5 mAh·g^{-1} (41st) to 185.8 mAh·g^{-1} (50th), which is higher than that of the hollow spherical Li_2FeSiO_4 (its maximum capacity was 168.1 mAh·g^{-1} at 0.1 C, and below 150 mAh·g^{-1} at 0.2 C) [30]. Additionally, a hollow

spherical Li_2FeSiO_4 prepared by a template-free method, delivered the capacity less than 120 mAh·g^{-1} (0.1 C, 1.5–4.8 V) [16], a Li_2FeSiO_4 prepared with a template 168.1 mAh·g^{-1} (0.1 C, 1.5–4.6 V) [30], and a spherical Li_2FeSiO_4 with a template 140 mAh·g^{-1} at 0.2 C [31]. As shown in Table S1, the hollow hemispherical Li_2FeSiO_4 prepared with an ascorbic acid-assisted template-free method had a good electrochemical performance.

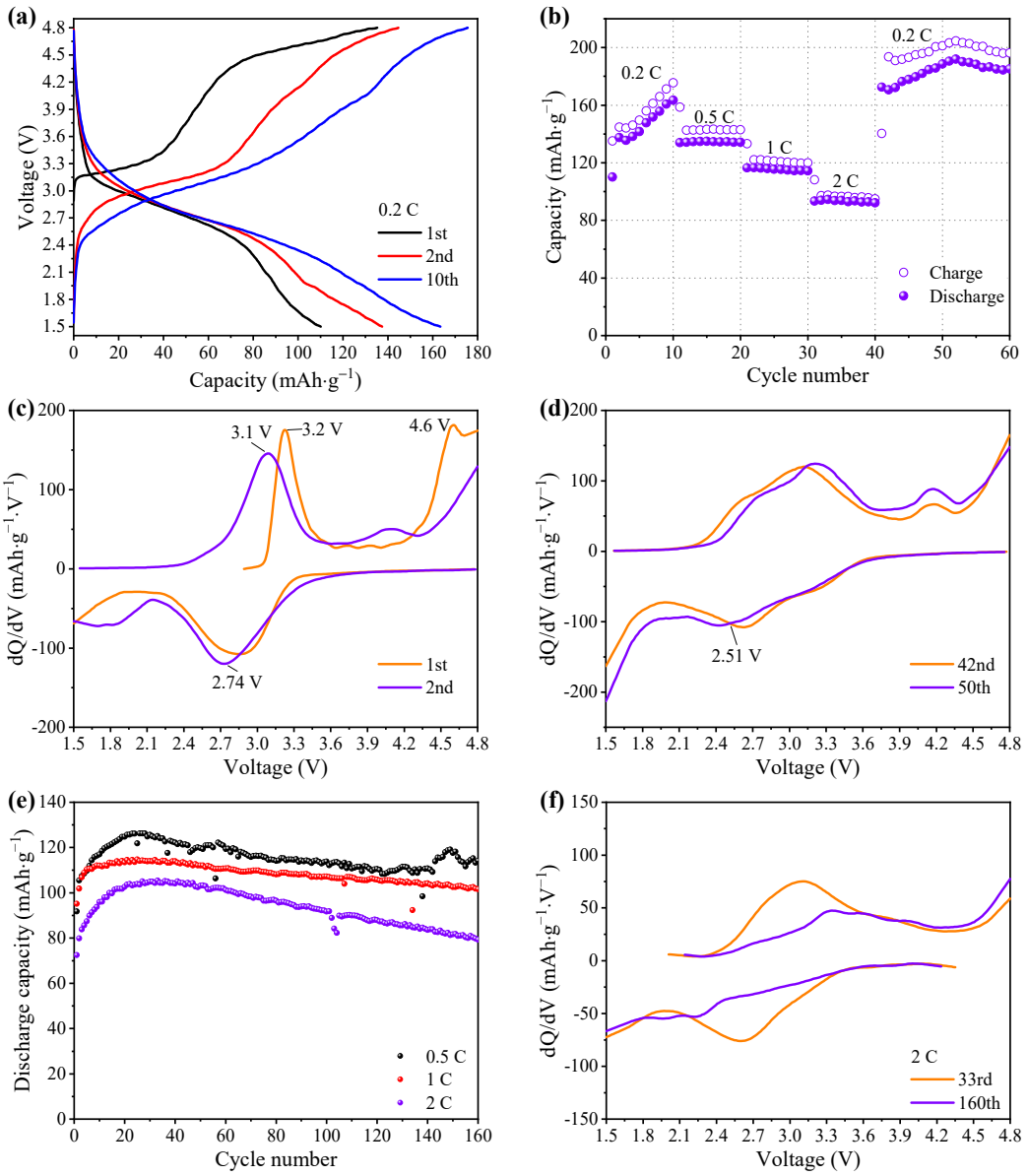

Figure 4. Electrochemical performance of the sample LFS600 at 1.5–4.8 V and 30 °C (**a**) Charge–discharge curves of the 1st, 2nd and 10th cycles at 0.2 C, (**b**) rate performance (1 C = 166 mA·g^{-1}), differential capacity curves of (**c**) the 1st and 2nd cycles, and (**d**) the 42nd and 50th cycles, (**e**) cycle performance at 0.5, 1 and 2 C, and (**f**) differential capacity curves for the 33rd and 160th cycles.

To analyze the reason for capacity increase from the 42nd cycle to the 50th cycle, differential capacity curves are compared in Figure 4d. The reduction curve of the 50th cycle has a greater |dQ/dV| value at 2.51–1.5 V than that of the 42nd cycle, indicating a faster reduction reaction at 2.51–1.5 V. This result reflects that the increase in capacity from the 42nd cycle to the 50th cycle is attributed to the accelerated reduction reaction at 2.51–1.5 V, caused by a side reduction [25,48,49] that is different from the reduction of Fe ions. The cycle performance in Figure 4e shows a capacity increase in the initial few cycles, which is similar to the capacity increase in the first 10 cycles in Figure 4b and is attributed to the decreased

polarization of the charge–discharge curve (Figure 4a). The essential reason for the capacity increase may be material activation and could be because the initial material is Li-poor $Li_{2-x}FeSiO_4$, which forms Li_2FeSiO_4 during cycling [47], or the increased wettability of the material by the electrolyte [16]. In the following cycles, the capacities at 0.5, 1 and 2 C decayed from the highest capacities of 126.2, 114.7 and 105.4 mAh·g^{-1} to 114.2, 101.6 and 79.3 mAh·g^{-1}, with the capacity retention rates of 90.5%, 88.6% and 75.2%, respectively. To understand the capacity decay, differential capacity curves of the 33rd and 160th cycles are compared in Figure 4f. The peak intensity of the 160th cycle curve is significantly reduced, indicating that the Fe^{2+}/Fe^{3+} redox reaction rate slows down, which may be related to the changes in the material structure and the chemical environment. The previous in-situ XRD results showed that Li_2FeSiO_4 undergoes a two-phase transition from Li_2FeSiO_4 to $LiFeSiO_4$, and from $LiFeSiO_4$ to Li_yFeSiO_4 ($0 \leq y < 1$) during the charging process [9,50]. Oxidation of oxygen occurs during the second phase transition [9], resulting in a larger structural change than the first phase transition. During the discharge process, a negligible change was observed on the XRD patterns up to a discharge voltage of 1.5 V [50]. After 10 cycles, the ratio of the monoclinic phase decreased, while the ratio of the orthorhombic phase increased in the two-phase mixed Li_2FeSiO_4 [8], indicating that the monoclinic phase may be transformed into the orthorhombic phase during cycling. After charging–discharging, a solid electrolyte interface (SEI) layer composed of an electrolyte redox product was formed on the surface of the Li film in the battery (Figure S3), indicating that the chemical environment in the battery has been changed, thus affecting the cycle performance.

To analyze the kinetic of the hollow hemispherical Li_2FeSiO_4, the electrical conductivity was further identified by EIS characterization, and a Nyquist plot of the LSF600 is shown in Figure 5a. The inset is an equivalent circuit that is used to fit the EIS data. In the circuit, CPE denotes the constant phase element, and is employed to fit the depressed semicircle (an arc). W stands for the Warburg impedance [30], R_Ω reflects the total resistance including the electrode, separator and electrolyte, and R_{ct} is the charge transfer resistance. Fitting the EIS data yields R_Ω = 4.75 Ω, and R_{ct} = 43.1 Ω. Figure 5b is a Z'-$\omega^{-1/2}$ ($\omega = 2\pi f$, f is the frequency) plot based on the linear part in Figure 5a, and the slope (σ) obtained by linear fitting can be used to calculate the Li ion diffusion coefficient (D_{Li^+}) according to the following equations [51–53].

$$D_{Li^+} = \frac{R^2T^2}{2A^2n^4F^4C_{Li^+}{}^2\sigma^2} \quad (1)$$

$$Z' = R_\Omega + R_{ct} + \sigma\omega^{-1/2} \quad (2)$$

where R is the gas constant (8.314 J·mol^{-1}·K^{-1}), T is the thermodynamic temperature (corresponding to 298.15 K at room temperature of 25 °C), A is the electrode surface area (1.96 cm^2), and n is the number of electron transfers in the redox process (n = 1) [30], F is Faraday's constant (96,483 C·mol^{-1}), representing the charge carried per mole of electrons, $F = e\,N_A$, e = 1.602176 × 10^{-19} C, N_A = 6.022 × 10^{23}, C_{Li^+} is the bulk concentration of Li ions in Li_2FeSiO_4 (0.04 0.04 mol/cm^3) [51–53]. Substitute the above values into Equation (1) to get the following:

$$D_{Li^+} = \frac{5.7680 \times 10^{-12}}{\sigma^2} \quad (3)$$

The calculated Li ion diffusion coefficient of the LFS600 is 2.53 × 10^{-16} cm^2·s^{-1}, which is close to 2.90 × 10^{-16} cm^2·s^{-1} for the graphene-modified Li_2FeSiO_4 [2].

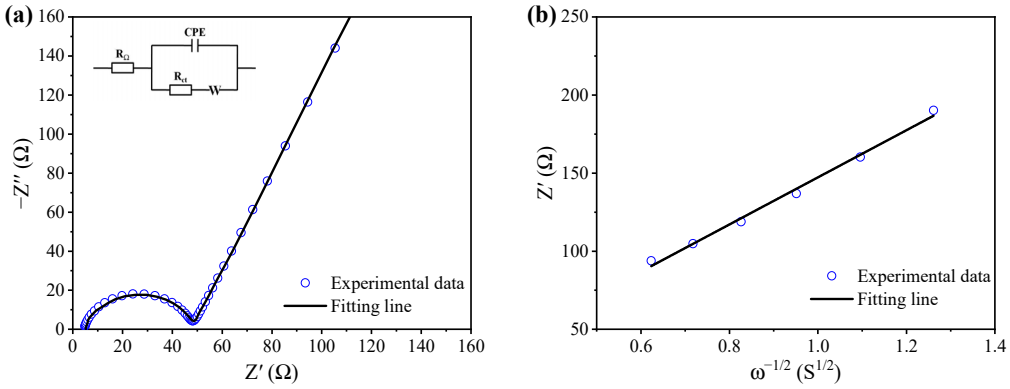

Figure 5. (**a**) Electrochemical impedance spectrum of the LFS600 under open circuit voltage, the inset is the equivalent circuit used to fit the data, and (**b**) linear fitting the data in the low frequency region of (**a**). The frequency values corresponding to the data points in (**b**) are 0.40949, 0.30888, 0.233, 0.17575, 0.13257, 0.1 Hz from left to right.

4. Conclusions

In summary, a hollow hemispherical Li_2FeSiO_4 was synthesized by a template-free hydrothermal method with the addition of ascorbic acid. In the presence of ascorbic acid, Li_2FeSiO_4 would finally grow into hollow hemispheres self-assembled by tiny nanoparticles. At different hydrothermal temperatures, the LFS160, LFS180 and LFS200 samples had different particle sizes, and the higher the temperature, the larger the particles. The carbon-coated LFS600 sample exhibited a high discharge capacity of 192 $mAh \cdot g^{-1}$ at 0.2 C, and the average capacities reached 134.5, 115.5 and 93.4 $mAh \cdot g^{-1}$ at 0.5, 1 and 2 C, respectively. Furthermore, the capacity increased with the cycle number in the first few cycles, and then decayed afterwards. From the perspective of redox analysis, the intuitive reason for the capacity decay is that the redox peak intensity of Fe ions decreased; that is, the redox activity was lowered. Adding ascorbic acid in the hydrothermal process could change the self-assembly behavior of the particles, which provides inspiration for the synthesis of Li_2FeSiO_4 nanoparticles with a tuned morphology and an enhanced performance.

Supplementary Materials: The following supporting information can be downloaded at: https://www.mdpi.com/article/10.3390/ma15103545/s1, Figure S1: Particle size distributions (a) LFS160, (b) LFS180 and (c) LFS200 samples based on 100 particles counted for each sample; Figure S2: Rate performances of LFS600 and nano-LFS600 samples obtained by the hydrothermal reaction with and without the addition of ascorbic acid, respectively; Figure S3: SEM image of the Li film in the charged–discharged LFS600 battery. The substances originated from the redox product at the electrolyte were deposited on the Li film to form an SEI layer; Table S1: Comparison in the maximum capacity of Li_2FeSiO_4/C with different spherical morphologies.

Author Contributions: H.L.: Conceptualization, Validation, Formal analysis, Investigation, Data curation, Writing—Original Draft, Writing—Review and Editing. Y.L.: Supervision, Writing—Review and Editing. X.C.: Resources, Supervision, Writing—Review and Editing. C.G.: Data curation. All authors have read and agreed to the published version of the manuscript.

Funding: This research was funded by the Natural Science Foundation of Shaanxi Province (2020JM-084), and the Basic Research Plan of Taicang City (TC2019JC07).

Institutional Review Board Statement: Not applicable.

Informed Consent Statement: Not applicable.

Data Availability Statement: The datasets generated during and/or analyzed during the current study are available from the corresponding author on reasonable request.

Conflicts of Interest: The authors declare no conflict of interest. The authors declare that they have no known competing financial interests or personal relationships that could have appeared to influence the work reported in this paper.

References

1. Lecce, D.D.; Verrellia, R.; Hassoun, J. Lithium-ion batteries for sustainable energy storage: Recent advances towards new cell configurations. *Green Chem.* **2017**, *19*, 3442–3467. [CrossRef]
2. Liu, T.; Liu, Y.; Yu, Y.; Ren, Y.; Sun, C.; Liu, Y.; Xu, J.; Liu, C.; Yang, Z.; Lu, W.; et al. Approaching theoretical specific capacity of iron-rich lithium iron silicate using graphene-incorporation and fluorine-doping. *J. Mater. Chem. A* **2022**, *10*, 4006–4014. [CrossRef]
3. Sasaki, H.; Nemoto, A.; Moriya, M.; Miyahara, M.; Hokazono, M.; Katayama, S.; Akimoto, Y.; Nakajima, A.; Hirano, S. Destruction behavior of carbon hybridized Li_2MnSiO_4 and Li_2FeSiO_4 nanoparticles for cathode materials. *Ceram. Int.* **2015**, *41*, S680–S685. [CrossRef]
4. Muraliganth, T.; Stroukoff, K.R.; Manthiram, A. Microwave-solvothermal synthesis of nanostructured Li_2MSiO_4/C (M = Mn and Fe) cathodes for lithium-ion batteries. *Chem. Mater.* **2010**, *22*, 5754–5761. [CrossRef]
5. Li, Y.X.; Gong, Z.L.; Yang, Y. Synthesis and characterization of Li_2MnSiO_4/C nanocomposite cathode material for lithium ion batteries. *J. Power Sources* **2007**, *174*, 528–532. [CrossRef]
6. Li, J.; Zhang, M.L.; Xue, T.T.; Zhang, D.Y.; Yan, Y.X.; Li, Z.M. Hydrothermal-assisted synthesis of Li_2FeSiO_4/C composites as cathode materials for lithium-ion batteries. *Int. J. Electrochem. Sci.* **2020**, *15*, 587–598. [CrossRef]
7. Chen, Z.; Qiu, S.; Cao, Y.; Qian, J.; Ai, X.; Xie, K.; Hong, X.; Yang, H. Hierarchical porous Li_2FeSiO_4/C composite with 2 Li storage capacity and long cycle stability for advanced Li-ion batteries. *J. Mater. Chem. A* **2013**, *1*, 4988–4992. [CrossRef]
8. Lu, X.; Chiu, H.C.; Arthur, Z.; Zhou, J.G.; Wang, J.; Chen, N.; Jiang, D.T.; Zaghib, K.; Demopoulos, G.P. Li-ion storage dynamics in metastable nanostructured Li_2FeSiO_4 cathode: Antisite-induced phase transition and lattice oxygen participation. *J. Power Sources* **2016**, *329*, 355–363. [CrossRef]
9. Masese, T.; Tassel, C.; Orikasa, Y.; Koyama, Y.; Arai, H.; Hayashi, N.; Kim, J.; Mori, T.; Yamamoto, K.; Kobayashi, Y.; et al. Crystal structural changes and charge compensation mechanism during two lithium extraction/insertion between Li_2FeSiO_4 and $FeSiO_4$. *J. Phys. Chem. C* **2015**, *119*, 10206–10211. [CrossRef]
10. Liu, J.Y.; Li, Y.H.; Yang, S.; Ai, J.J.; Lai, C.Y.; Xu, Q.J. Improved cycling performance and rate stability of ITO-compounded Li_2MnSiO_4 for lithium-ion batteries. *RSC Adv.* **2018**, *8*, 9795–9801. [CrossRef]
11. Li, Y.; Cheng, X.; Zhang, Y. Achieving high capacity by vanadium substitution into Li_2FeSiO_4. *J. Electrochem. Soc.* **2012**, *159*, A69–A74. [CrossRef]
12. Kumar, A.; Jayakumar, O.D.; Jagannath; Bashiri, P.; Nazri, G.A.; Naik, V.M.; Naik, R. Mg doped Li_2FeSiO_4/C nanocomposites synthesized by the solvothermal method for lithium ion batteries. *Dalton Trans.* **2017**, *46*, 12908–12915. [CrossRef] [PubMed]
13. Qu, L.; Li, M.; Tian, X.; Liu, P.; Yi, Y.; Yang, B. Calcium cation enhanced cathode/electrolyte interface property of Li_2FeSiO_4/C cathode for lithium-ion batteries with long-cycling life. *Chem. Phys.* **2018**, *503*, 1–13. [CrossRef]
14. Qu, L.; Li, M.; Bian, L.; Du, Q.; Luo, M.; Yang, B.; Yang, L.; Fang, S.; Liu, Y. A strontium-doped Li_2FeSiO_4/C cathode with enhanced performance for the lithium-ion battery. *J. Solid State Electrochem.* **2017**, *21*, 3659–3673. [CrossRef]
15. Lee, J.J.; Dinh, H.C.; Mho, S.I.; Yeo, I.H.; Cho, W.I.; Kim, D.W. Morphology-controlled solvothermal synthesis of Li_2FeSiO_4 nanoparticles for Li-ion battery cathodes. *Mater. Lett.* **2015**, *160*, 507–510. [CrossRef]
16. Xu, Y.; Shen, W.; Zhang, A.; Liu, H.; Ma, Z. Template-free hydrothermal synthesis of Li_2FeSiO_4 hollow spheres as cathode materials for lithium-ion batteries. *J. Mater. Chem. A* **2014**, *2*, 12982–12990. [CrossRef]
17. Yi, L.L.; Wang, G.; Bai, Y.S.; Liu, M.H.; Wang, X.; Liu, M.; Wang, X.Y. The effects of morphology and size on performances of Li_2FeSiO_4/C cathode materials. *J. Alloys Compd.* **2017**, *721*, 683–690. [CrossRef]
18. Vajeeston, P. Ionic conductivity enhancement by particle size reduction in Li_2FeSiO_4. *Mater. Lett.* **2018**, *218*, 313–316. [CrossRef]
19. Cui, J.; Qing, C.; Zhang, Q.; Su, C.; Wang, X.; Yang, B.; Huang, X. Effect of the particle size on the electrochemical performance of nano-Li_2FeSiO_4/C composites. *Ionics* **2014**, *20*, 23–28. [CrossRef]
20. Wang, K.; Ren, W.J.; Yang, J.L.; Tan, R.; Liu, Y.D.; Pan, F. Depolarization effects of Li_2FeSiO_4 nanocrystals wrapped in different conductive carbon networks as cathodes for high performance lithium-ion batteries. *RSC Adv.* **2016**, *6*, 47723–47729. [CrossRef]
21. Thayumanasundaram, S.; Rangasamy, V.S.; Seo, J.W.; Locquet, J.-P. A combined approach: Polyol synthesis of nanocrystalline Li_2FeSiO_4, doping multi-walled carbon nanotubes, and ionic liquid electrolyte to enhance cathode performance in Li-ion batteries. *Electrochim. Acta* **2017**, *258*, 1044–1052. [CrossRef]
22. Huang, B.; Zheng, X.; Lu, M. Synthesis and electrochemical properties of carbon nano-tubes modified spherical Li_2FeSiO_4 cathode material for lithium-ion batteries. *J. Alloys Compd.* **2012**, *525*, 110–113. [CrossRef]
23. Wang, W.C.; Liang, H.C.; Zhang, L.; Savilov, S.V.; Ni, J.F.; Li, L. Carbon nanotube directed three-dimensional porous Li_2FeSiO_4 composite for lithium batteries. *Nano Res.* **2017**, *10*, 229–237. [CrossRef]
24. Zhang, Z.; Liu, X.Q.; Wang, L.P.; Wu, Y.; Zhao, H.Y.; Chen, B.; Xiong, W.Q. Fabrication and characterization of carbon-coated Li_2FeSiO_4 nanoparticles reinforced by carbon nanotubes as high performance cathode materials for lithium-ion batteries. *Electrochim. Acta* **2015**, *168*, 8–15. [CrossRef]
25. Singh, S.; Mitra, S. Improved electrochemical activity of nanostructured Li_2FeSiO_4/MWCNTs composite cathode. *Electrochim. Acta* **2014**, *123*, 378–386. [CrossRef]
26. Zhao, Y.; Li, J.; Wang, N.; Wu, C.; Ding, Y.; Guan, L. In situ generation of Li_2FeSiO_4 coating on MWNT as a high rate cathode material for lithium ion batteries. *J. Mater. Chem.* **2012**, *22*, 18797–18800. [CrossRef]
27. Ni, J.F.; Jiang, Y.; Bi, X.X.; Li, L.; Lu, J. Lithium iron orthosilicate cathode: Progress and perspectives. *ACS Energy Lett.* **2017**, *2*, 1771–1781. [CrossRef]

28. Liang, J.; Kou, H.; Ding, S. Complex hollow bowl-like nanostructures: Synthesis, application, and perspective. *Adv. Funct. Mater.* **2021**, *31*, 2007801. [CrossRef]
29. Zhu, X.; Tang, J.; Huang, H.; Lin, T.; Luo, B.; Wang, L. Hollow structured cathode materials for rechargeable batteries. *Sci. Bull.* **2020**, *65*, 496–512. [CrossRef]
30. Shen, S.Y.; Zhang, Y.; Wei, G.H.; Zhang, W.S.; Yan, X.H.; Xia, G.F.; Wu, A.M.; Ke, C.C.; Zhang, J.L. Li_2FeSiO_4/C hollow nanospheres as cathode materials for lithium-ion batteries. *Nano Res.* **2019**, *12*, 357–363. [CrossRef]
31. Qu, L.; Fang, S.; Yang, L.; Hirano, S.-i. Li_2FeSiO_4/C cathode material synthesized by template-assisted sol-gel process with Fe_2O_3 microsphere. *J. Power Sources* **2012**, *217*, 243–247. [CrossRef]
32. Ren, B.; Xu, Y.; Yan, Y.; Yang, R.; Wang, J. Synthesis and electrochemical performance of spherical-like Li_2FeSiO_4/C/SP cathode material for lithium-ion batteries. *J. Alloy Compd.* **2015**, *633*, 456–462. [CrossRef]
33. Huang, X.; You, Y.; Ren, Y.; Wang, H.; Chen, Y.; Ding, X.; Liu, B.; Zhou, S.; Chu, F. Spray drying-assisted synthesis of hollow spherical Li_2FeSiO_4/C particles with high performance for Li-ion batteries. *Solid State Ion.* **2015**, *278*, 203–208. [CrossRef]
34. Zeng, Y.; Chiu, H.-C.; Rasool, M.; Brodusch, N.; Gauvin, R.; Jiang, D.-T.; Ryan, D.H.; Zaghib, K.; Demopoulos, G.P. Hydrothermal crystallization of $Pmn2_1$ Li_2FeSiO_4 hollow mesocrystals for Li-ion cathode application. *Chem. Eng. J.* **2019**, *359*, 1592–1602. [CrossRef]
35. Li, M.; Zhang, L.-L.; Yang, X.-L.; Huang, Y.-H.; Sun, H.-B.; Ni, S.-B.; Tao, H.-C. Synthesis and electrochemical performance of Li_2FeSiO_4/C cathode material using ascorbic acid as an additive. *J. Solid State Electrochem.* **2015**, *19*, 415–421. [CrossRef]
36. Yang, J.; Hu, L.; Zheng, J.; He, D.; Tian, L.; Mu, S.; Pan, F. Li_2FeSiO_4 nanorods bonded with graphene for high performance batteries. *J. Mater. Chem. A* **2015**, *3*, 9601–9608. [CrossRef]
37. Sirisopanaporn, C.; Masquelier, C.; Bruce, P.G.; Armstrong, A.R.; Dominko, R. Dependence of Li_2FeSiO_4 electrochemistry on structure. *J. Am. Chem. Soc.* **2011**, *133*, 1263–1265. [CrossRef]
38. Qin, Y.Q.; Ji, X.H.; Jing, J.; Liu, H.; Wu, H.L.; Yang, W.S. Size control over spherical silver nanoparticles by ascorbic acid reduction. *Colloid Surf. A* **2010**, *372*, 172–176. [CrossRef]
39. Xu, Y.; Shen, W.; Wang, C.; Zhang, A.; Xu, Q.; Liu, H.; Wang, Y.; Xia, Y. Hydrothermal synthesis and electrochemical performance of nanoparticle Li_2FeSiO_4/C cathode materials for lithium ion batteries. *Electrochim. Acta* **2015**, *167*, 340–347. [CrossRef]
40. Jiang, X.; Xu, H.; Yang, J.; Liu, J.; Mao, H.; Qian, Y. Synthesis of novel morphologies of Li_2FeSiO_4/C micro/nano composites by a facile hydrothermal method. *RSC Adv.* **2014**, *4*, 39889–39893. [CrossRef]
41. Gao, H.; Hu, Z.; Zhang, K.; Cheng, F.; Tao, Z.; Chen, J. Hydrothermal synthesis of spindle-like Li_2FeSiO_4-C composite as cathode materials for lithium-ion batteries. *J. Energy Chem.* **2014**, *23*, 274–281. [CrossRef]
42. Lv, D.; Wen, W.; Huang, X.; Bai, J.; Mi, J.; Wu, S.; Yang, Y. A novel Li_2FeSiO_4/C composite: Synthesis, characterization and high storage capacity. *J. Mater. Chem.* **2011**, *21*, 9506–9512. [CrossRef]
43. Kojima, A.; Kojima, T.; Tabuchi, M.; Sakai, T. Crystal structure and electrochemical performance of a new lithium trivalent iron silicate. *J. Electrochem. Soc.* **2012**, *159*, A725–A729. [CrossRef]
44. Wang, Y.J.; Wu, Y.; Yang, F.; Wang, J.; Zhou, J.C. An active-oxygen-scavenging oriented cathode-electrolyte-interphase for long-life lithium-rich cathode materials. *Small* **2022**, *18*, 2106072. [CrossRef]
45. Guerrini, N.; Jin, L.; Lozano, J.G.; Luo, K.; Sobkowiak, A.; Tsuruta, K.; Massel, F.; Duda, L.-C.; Roberts, M.R.; Bruce, P.G. Charging mechanism of Li_2MnO_3. *Chem. Mater.* **2020**, *32*, 3733–3740. [CrossRef]
46. Luo, M.Z.; Zheng, S.Y.; Wu, J.; Zhou, K.; Zuo, W.H.; Feng, M.; He, H.J.; Liu, R.; Zhu, J.P.; Zhao, G.; et al. Identifying the anionic redox activity in cation-disordered $Li_{1.25}Nb_{0.25}Fe_{0.50}O_2$/C oxide cathodes for Li-ion batteries. *J. Mater. Chem. A* **2020**, *8*, 5115–5127. [CrossRef]
47. Fujita, Y.; Iwase, H.; Shida, K.; Liao, J.S.; Fukui, T.; Matsuda, M. Synthesis of high-performance Li_2FeSiO_4/C composite powder by spray-freezing/freeze-drying a solution with two carbon sources. *J. Power Sources* **2017**, *361*, 115–121. [CrossRef]
48. Du, X.; Zhao, H.; Lu, Y.; Gao, C.; Xia, Q.; Zhang, Z. Electrochemical properties of nanostructured Li_2FeSiO_4/C synthesized by a simple co-precipitation method. *Electrochim. Acta* **2016**, *188*, 744–751. [CrossRef]
49. Nyten, A.; Abouimrane, A.; Armand, M.; Gustafsson, T.; Thomas, J.O. Electrochemical performance of Li_2FeSiO_4 as a new Li-battery cathode material. *Electrochem. Commun.* **2005**, *7*, 156–160. [CrossRef]
50. Lv, D.; Bai, J.; Zhang, P.; Wu, S.; Li, Y.; Wen, W.; Jiang, Z.; Mi, J.; Zhu, Z.; Yang, Y. Understanding the high capacity of Li_2FeSiO_4: In situ XRD/XANES study combined with first-principles calculations. *Chem. Mater.* **2013**, *25*, 2014–2020. [CrossRef]
51. Qu, L.; Liu, Y.; Fang, S.; Yang, L.; Hirano, S.-i. Li_2FeSiO_4 coated by sorbitanlaurat-derived carbon as cathode of high-performance lithium-ion battery. *Electrochim. Acta* **2015**, *163*, 123–131. [CrossRef]
52. Singh, S.; Raj, A.K.; Sen, R.; Johari, P.; Mitra, S. Impact of Cl doping on electrochemical performance in orthosilicate (Li_2FeSiO_4): A density functional theory supported experimental approach. *ACS Appl. Mater. Interfaces* **2017**, *9*, 26885–26896. [CrossRef] [PubMed]
53. Li, D.L.; Zhang, W.; Sun, R.; Yong, H.T.H.; Chen, G.Q.; Fan, X.Y.; Gou, L.; Mao, Y.Y.; Zhao, K.; Tian, M. Soft-template construction of three-dimensionally ordered inverse opal structure from Li_2FeSiO_4/C composite nanofibers for high-rate lithium-ion batteries. *Nanoscale* **2016**, *8*, 12202–12214. [CrossRef] [PubMed]